Journal of Nuclear Materials 509 (2018) 162–167

Contents lists available at ScienceDirect

Journal of Nuclear Materials

journal homepage: www.elsevier.com/locate/jnucmat

Experimental determination of zirconium hydride precipitation and dissolution in zirconium alloy

E. Lacroix [a, *], A.T. Motta [a], J.D. Almer [b]

[a] Department of Mechanical and Nuclear Engineering, The Pennsylvania State University, University Park, PA, 16802, USA
[b] Advanced Photon Source, Argonne National Laboratory, Argonne, IL, 60439, USA

ARTICLE INFO

Article history:
Received 13 December 2017
Received in revised form
8 June 2018
Accepted 22 June 2018
Available online 23 June 2018

ABSTRACT

Synchrotron X-Ray transmission diffraction experiments were performed to study hydride precipitation and dissolution in the zirconium/zirconium-hydride system while it occurs. Evidence was found that the hysteresis between the terminal solid solubility for precipitation and dissolution is not observed when hydride particles are already present at the beginning of sample cooldown. Furthermore, experimental results show that, during a temperature hold, the concentration of hydrogen in solid solution becomes lower than the terminal solid solubility for hydride *precipitation* and eventually reaches the terminal solid solubility for hydride *dissolution*, indicating that the latter is the actual thermodynamic solubility limit.

1. Introduction

The ingress of hydrogen into nuclear fuel rod cladding during operation and the precipitation of brittle hydride particles can reduce cladding ductility [1,2]. Because of this, in addition to studying hydrogen pickup during corrosion, it is important to study the processes of hydrogen transport and hydride precipitation once the hydrogen enters the cladding. A model of hydrogen transport and hydride precipitation was proposed by Courty et al. [3], based on known processes of hydrogen mobility in the cladding, driven by both a concentration and a temperature gradient. The hydride precipitation and dissolution model in that study was based simply on the terminal solid solubilities for dissolution and precipitation [4] and on the kinetic model introduced by Marino [5]. The proposed model is summarized in Table 1.

In Table 1, C_{SS} is the hydrogen content in solid solution (in wt. ppm), C_P is the hydrogen in hydrides (in wt. ppm), TSS_P and TSS_D are the terminal solid solubilities for hydride precipitation and dissolution respectively (both expressed in wt. ppm), α^2 is the precipitation kinetics parameter, β^2 is the dissolution kinetics parameter (both in s^{-1}) and J is the hydrogen diffusion flux (wt.ppm/cm^2/s). While TSS_P, TSS_D and α^2 are determined experimentally, β^2 was assumed to be equal to 1 as hydride dissolution is fast [3]. α^2 was measured experimentally by Kammenzind [6] and by Courty et al. in Ref. [7]. Since it was considered that a stress gradient was less influential than the other gradients, the hydrogen flux J, which leads to hydrogen redistribution, depends mainly on two physical phenomena: Fick's law of diffusion and thermodiffusion (the Soret effect).

$$J_{Diff} = -D\nabla C_{SS} - \frac{DQ^* C_{SS}}{RT^2}\nabla T \quad (1)$$

where D is the diffusion coefficient of hydrogen in Zircaloy (in m^2/s), Q^* the heat of transport (in J/mol), R the ideal gas constant (in J/mol/Kelvin) and T the temperature (in Kelvin). Although this model was implemented into the finite element code BISON and used to determine the hydrogen concentration in service, questions remain as to whether all the physics involved are properly considered.

The hydrogen solubility limits in precipitation and dissolution have been measured by several authors, who have in general reported a hysteresis between precipitation and dissolution [4,8–13]. However, previous results suggest that the hysteresis may not be present when hydrides are already precipitated at the start of cooldown [11]. Therefore, a better understanding of the hydride precipitation/dissolution hysteresis in this system is needed to understand these processes and to discern which of the two solubility limits is a true thermodynamic limit, rather than a kinetic effect. A series of experiments were therefore specifically designed to clarify these issues.

* Corresponding author.
E-mail address: eul152@psu.edu (E. Lacroix).

https://doi.org/10.1016/j.jnucmat.2018.06.038
0022-3115/

Table 1
Model for hydrogen precipitation and dissolution [3].

Conditions	Model
if $C_{SS} > TSS_P$ *and* $C_P \geq 0$	$\begin{cases} \frac{dC_P}{dt} = \alpha^2(C_{SS} - TSS_P) \\ \frac{dC_{SS}}{dt} = -\nabla J - \alpha^2(C_{SS} - TSS_P) \end{cases}$
if $C_{SS} < TSS_D$ *and* $C_P > 0$	$\begin{cases} \frac{dC_P}{dt} = -\beta^2(TSS_D - C_{SS}) \\ \frac{dC_{SS}}{dt} = -\nabla J + \beta^2(TSS_D - C_{SS}) \end{cases}$
if $C_{SS} < TSS_D$ *and* $C_P = 0$ *or if* $TSS_D \leq C_{SS} < TSS_P$ *and* $C_P \geq 0$	$\begin{cases} \frac{dC_P}{dt} = 0 \\ \frac{dC_{SS}}{dt} = -\nabla J \end{cases}$

2. Experimental methods

The material used for this experiment was cold-worked stress-relieved (CWSR) Zircaloy-4 sheet provided by ATI Specialty Alloys and Components. The material texture was such that the basal poles were inclined approximately ±30° away from the normal direction of the sheet [14,15]. The Kearns factors [16] were measured to be $f_N = 0.59$, $f_L = 0.05$ and $f_T = 0.31$ in the normal, longitudinal and transverse directions respectively. These values are similar to those normally obtained in CWSR Zircaloy-4 cladding [17].

The material was hydrided using gaseous charging in an atmosphere of 1% hydrogen and 99% argon. Prior to gaseous charging, samples were etched with a solution of 10% Hydrofluoric Acid (49% concentrated), 45% Nitric Acid (79% concentrated) and 45% deionized water to remove the native oxide layer. A 20 nm layer of Nickel was then sputtered onto the etched surface to protect it against air corrosion, using a Kurt J. Lesker CMS (Combinatorial Material Science) series sputter machine. Hydriding by gaseous charging was performed by first creating a secondary vacuum (~10^{-6} Torr) and then introducing the desired amount of hydrogen into the loading chamber. The loading chamber was heated to 450 °C to allow hydrogen absorption and diffusion while ensuring that the absorbed hydrogen remain in solid solution. Once the target temperature and vacuum was reached, the control volume valve was opened and hydrogen was released into the loading chamber. The system remained as such for 2 h to allow hydrogen to be absorbed and to diffuse into the material. The hydrogen content in the sample studied after gas charging was measured to be 255 ± 43 wt. ppm by Luvak Inc., using Vacuum Hot Extraction (in accordance with ASTM E146). The hydrided sheet was then machined into a uniaxial testing dog-bone configuration using wire electrical discharge machining. The sample geometry is shown in Fig. 1a. This sample was examined at the 1-ID-E beamline at the Advanced Photon Source at Argonne National Laboratory using an 80.725 keV X-ray beam capable of completely penetrating through a 0.6 mm thick sample. The beam size was 100 × 100 μm. The diffraction patterns generated were recorded using a GE 41RT area detector, while the sample was heated and cooled in a furnace, as shown schematically in Fig. 1b.

The diffraction pattern showed peaks that could be indexed as coming from both the Zr matrix and the hydride phase. As in other studies we performed, only peaks associated with the delta hydride phase were observed – no peaks from other hydride phases such as γ, ε or ζ were observed. The intensity of the δ(111) hydride diffraction peak was used as a gauge of the hydride volume fraction in the sample. Accordingly, the evolution of the δ(111) hydride peak integrated intensity with respect to time and temperature was determined by recording a diffraction pattern every 16 s and determining the integrated intensity under the peak. The diffraction patterns were obtained by summing over 18 diffraction patterns taken for 0.5 s each. The time per pattern was chosen to avoid detector saturation from the strongest zirconium peaks, and the summation provided sufficient signal-to-noise ratio for the hydride peaks. The δ(111) hydride peak intensity was obtained by integrating along the full diffraction ring. Because the δ(111) hydride peak is located at the tail of the stronger $(10\bar{1}0)$ Zr peak, it was necessary to fit these together as a pair of Pseudo Voigt functions.

The integrated peak intensity of the δ(111) hydride at each time step of this heat treatment was one of the parameters extracted from the pseudo-voigt fits. The integrated δ(111) hydride diffracted intensity is related to the hydrogen content in solid solution by:

$$C_{SS}(t) = C_{VHE}\left(1 - \frac{I(t)}{I_m}\right) \quad (2)$$

were $C_{SS}(t)$ is the hydrogen content in solid solution at time t, C_{VHE} is the total hydrogen content measured using Vacuum Hot Extraction, I(t) is the integrated intensity of the δ(111) hydride peak at time t and I_m is the intensity of the δ(111) hydride diffraction peak when the hydrides are fully precipitated. Equation (2) assumes that the hydride texture does not vary significantly during precipitation and dissolution so that the δ(111) hydride peak is a valid measure of the hydride volume fraction. This assumption was partly verified during the experiment. The (111) δ-hydride peak intensity was measured as a function of the chi angle of the diffraction ring at the beginning and the end of the experiment and no significant difference was observed, suggesting that the texture remained the same during the experiments. Also the integration of the diffracted intensity over the chi angle showed a constant value during the experiment, suggesting that little hydrogen was lost from the sample.

The type K thermocouple used by design yields a measurement error corresponding to the largest of 2.2 °C or 0.75% of the recorded

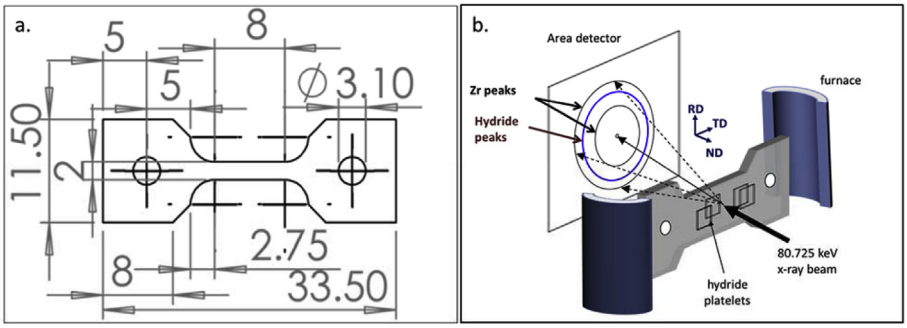

Fig. 1. (a) Dog-bone tensile testing sample dimensions (dimensions in mm), (b) Schematic depiction of the experimental setup at APS after [7].